

Pulse Shape Analysis and Identification of Multipoint Events in a Large-Volume Proportional Counter in an Experimental Search for 2K Capture ^{78}Kr

Yu.M. Gavriljuk,¹ A.M. Gangapshev,¹ V.V. Kazalov,¹ V.V. Kuzminov,¹
S.I. Panasenko,² S.S. Ratkevich,² and S. P. Yakimenko¹

¹*Baksan Neutrino Observatory INR RAS, Russia*

²*V.N.Karazin Kharkiv National University, Ukraine*

A pulse shape analysis algorithm and a method for suppressing the noise component of signals from a large copper proportional counter in the experiment aimed at searching for 2K capture of ^{78}Kr are described. These signals correspond to a compound event with different numbers of charge clusters due to from primary ionization is formed by these signals. A technique for separating single- and multipoint events and determining the charge in individual clusters is presented. Using the Daubechies wavelets in multiresolutional signal analysis, it is possible to increase the sensitivity and the resolution in extraction of multipoint events in the detector by a factor of $3 \div 4$.

PACS numbers: 29.30.Kv, 23.40.-s, 29.40.Cs, 98.70.Vc, 94.05.Rx, 07.05.Kf

I. INTRODUCTION

The main modern achievements in studying processes of double beta decay ($\beta^-\beta^-$ -decay) can be attributed to detection of its two-neutrino mode. This process has been discovered in as many as ten nuclei (see reviews [1],[2],[3]). The data obtained for the two-neutrino mode offer a chance to directly compare different models of the nuclear structure, which form the basis for calculations of nuclear matrix elements $\|M^{2\nu}\|$, and to select the optimal one. Though direct correlation between the values of nuclear matrix elements for the two-neutrino and neutrinoless modes of $\beta\beta$ decay is absent lacking, the methods for calculating $\|M^{2\nu}\|$ and $\|M^{0\nu}\|$ are very close, and a chance possibility to estimate their accuracy in calculating $\|M^{0\nu}\|$ appears only when comparing experimental data and theoretical results calculations for the probability of $2\beta(2\nu)$ decay.

It can be expected that acquisition of experimental data on the other types of 2β transitions ($2\beta^+$, $K\beta^+$, and $2K$ processes) will make it possible to considerably increase the quality of calculations for both 2ν and 0ν decays. Much efforts have been currently made in searching for these processes ([4],[5],[6]) in spite of the fact that the $2\beta^+(2\nu)$ and $K\beta^+(2\nu)$ modes are strongly suppressed relative to $2\beta(2\nu)$ decay due to the Coulomb barrier for positrons, and a substantially lower kinetic energy attainable in such transitions. Positrons are absent in the final state of the $2K(2\nu)$ decay, and the kinetic energy of the transition may be rather high (up to 2.8 MeV), which dictates determines an increased probability of a decay. However, this process is also difficult to detect, since it is only characteristic radiation that is detectable in it. The state-of-the-art experimental limit on the ^{78}Kr half-life period with respect to the $2K(2\nu)$ capture is $T_{1/2} \leq 1.5 \times 10^{21}$ yr (90% C.L.) [7]. The theoretical calculations based on different models predict the following ^{78}Kr half-lives for this process: 3.7×10^{21} yr [8], 4.7×10^{22} yr [9], and 7.9×10^{23} yr [10]. The last two values were obtained from the estimates of the ^{78}Kr half-life with re-

spect to the total number of $2e(2\nu)$ captures including in view of the 78.6% fraction of $2K(2\nu)$ capture events which makes 78.6% [11]. From comparison of the experimental and theoretical results, it is apparent that the sensitivity of measurements has reached the lower limit of theoretical estimates.

II. THE TECHNIQUE OF THE EXPERIMENT

The $^{78}\text{Kr}(2e_K, 2\nu)^{78}\text{Se}$ reaction produces a $^{78}\text{Se}^{**}$ atom with two vacancies in its K -shell. The technique for seeking this reaction is based on the assumption that the values of energies of characteristic photons, and of the probability that they will be emitted when the double vacancy is being filled, coincide with the corresponding values when two separate single vacancies in the K shells of two isolated singly ionized Se^* atoms are being filled. In this case, the total measured energy is $2K_{ab} = 25.3$ keV, where K_{ab} is the binding energy of a K electron in a Se atom (12.65 keV). The fluorescence yield upon filling of a single vacancy in the K -shell of Se is 0.596. The energies and relative intensities of the characteristic lines in the K series are $K = 11.22$ keV (100%), $K = 11.18$ keV (52%), $K = 12.49$ keV (21%), and $K = 12.65$ keV (1%) [12]. There are three possible ways for deexcitation of a doubly ionized K -shell: 1) emission of Auger electrons only (e_a, e_a), 2) emission of a single characteristic quantum and an Auger electron (K, e_a), and 3) emission of two characteristic quanta and low-energy Auger electrons (K, K, e_a), with probabilities $p_1 = 0.163$, $p_2 = 0.482$, and $p_3 = 0.355$, respectively. A characteristic quantum can travel a long enough distance in a gas medium between the points of its production and absorption. For example, 10% of characteristic quanta with energies of 11.2 and 12.5 keV is absorbed in krypton at a pressure of 4.35 atm ($\rho = 0.0164$ g/cm³) on a path 1.83 and 2.42 mm long, respectively (the values of absorption factors are taken from [13]). The paths of photoelectrons with the same energies are 0.37 and 0.44 mm, respec-

tively. They produce almost pointwise charge clusters of primary ionization in the gas. In case of the event with the escape of two characteristic quanta absorbed in the working gas and a single Auger electron, the energy will be distributed among three pointwise charge clusters. It is these three-point (or three-cluster) events possessing a unique set of features that were the subject of the search in [7].

A large proportional counter (LPC) with a casing made of M1-grade copper is used to detect the above considered processes. The LPC has a cylindrical shape with inner and outer diameters of 140 and 150 mm, respectively; its section along the axis is schematically shown in Fig.1. A gold-plated tungsten wire of $10\ \mu\text{m}$ in diameter goes along the LPC axis and serves as the anode. The potential of $+2400$ is applied to the wire, and the casing (the cathode) is grounded. Both ends of the anode are lead to the appropriate end cap flanges via high-voltage pressure-sealed bushings-ceramic insulators with a central electrode taken from spark plugs.

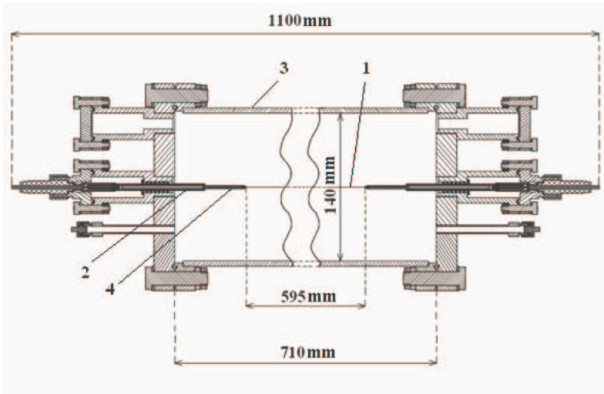


FIG. 1: Schematic view of the LPC in section along the anode wire: 1 – wire (collecting electrode), 2 – load-carrying insulator, 3 – cathode, 4 – tubular bulge of the anode.

To reduce the influence of edge effects on the operating characteristics of the counter, the end segments of the wire are passed through the copper tubes with dimensions of 3.0×38.5 mm, which are electrically connected to the anode. Gas amplification is absent on these segments, and charges are collected in an ionization mode. With the fluoroplastic insulator, the distance from the working region to the flange is 70 mm.

The working part of the LPC is 595 mm in length (the distance between the end caps of the tubes); therefore, the LPC's operating volume is 9,159 l. The total capacitance of the counter and the outlet insulator is 30.6 pF. The total resistance of the anode and two output electrodes is 600 Ω . All detachable joints are sealed with indium wire. All nipple joints are sealed with fluoroplastic gaskets. The internal insulators are made of fluoroplastic. Their thickness was selected so as to be the smallest possible in order to improve the degassing conditions during vacuum treatment of the counter and stabilize its

operating characteristics in the course of measurements.

The LPC is filled with a pure Kr sample to a total pressure of 4.51 att; no quenching or accelerating gases are added. Prior to filling, Kr is purified of electronegative impurities in a Ni/SiO₂ reactor.

The LPS's signals are read out by a charge-sensitive amplifier (CSA) from one end of the anode wire. The CSA parameters have been selected so that the signal is transmitted with minimum distortions, and information of the spatial distribution of primary-ionization charges in a projection onto a counter radius is fully represented by the pulse shape. When amplified in an auxiliary amplifier, the pulses arrive at the input of the digital oscilloscope LA-n20-12PCI, the output data of which (the pulse waveform digitized with a frequency of 6.25 MHz) are recorded with a personal computer. The length of the scanning frame with a resolution of 160 ns is 1024 points (163.8 μs), of which 50 μs is the "prehistory" and 114 μs is the "history".

The counter is calibrated through the wall of its casing by γ rays of a ^{109}Cd source ($E_\gamma = 88$ keV; relative yield 0.036 photons/decay). Figure 2 presents (0) the total pulse amplitude spectrum and the energy spectra of (1) single-, (2) two-, and (3) three-point events from the source located in the middle of the LPC length. The procedure for obtaining them from digitized pulses is described in what follows. The following factors make their contribution to the low-energy part of the spectrum: characteristic radiation $\text{Ag}_{K\alpha\beta}$ ($E \approx 22$ keV) from this source, which "survived" after passing through a 5-mm-thick copper wall; scattered radiation from the wall, which is in equilibrium with the characteristic radiation, and Compton electrons from scattering of 88-keV photons in the gas with the escape of a Compton photon beyond the counter.

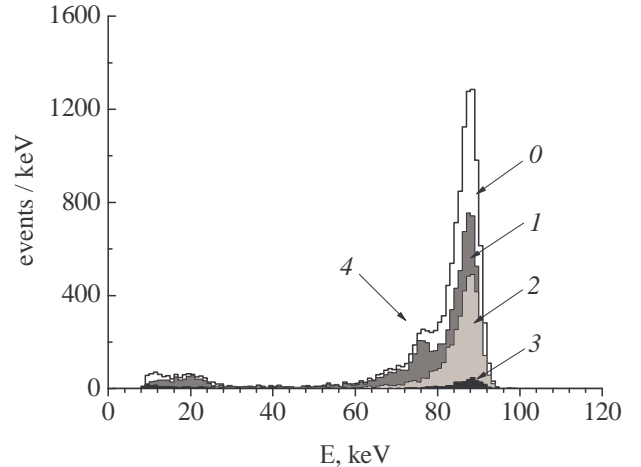


FIG. 2: Pulse amplitude spectrum from the external ^{109}Cd source located in the middle of the LPC length: (0) all events, (1) single-point events, (2) two-point events, (3) three-point events, and (4) escape peak of characteristic γ -ray photons.

The 88-keV peak is wider on the low-energy side due

to the contribution of 88-keV γ rays scattered from the wall. The energy resolution of this peak, determined by its right half, is 6.5%. Peak 4 at an energy of 75.4 keV corresponds to the escape of Kr characteristic radiation ($E_{Kr\alpha} = 12.6$ keV) beyond the counter.

The 88-keV full-energy peak contains events with different internal structures. Quanta with this energy are absorbed in Kr mostly by photoeffect in the K -shell (86.7%). The photoeffect in other shells makes 13.3% [13], [14]. Filling of the vacancy in the K -shell of Kr is accompanied by emission of characteristic radiation in 66.0% of cases and Auger electrons in 34.0% [14]. The theoretical efficiency of characteristic radiation absorption in the counter's working volume is 86.9%. Therefore, the photoeffect is responsible for 49.7% of two-point events ($0.867 \times 0.660 \times 0.869$) and 42.8% of single-point events ($0.133 + 0.867 \times 0.340$) out of the total number of absorptions due to photoeffect in the full-energy peak. By single-point events, we mean all events in which only electrons escaping from the shell of a single atom (photoelectrons + Auger electrons), including events of photoelectric absorption in the upper shells of Kr. Only single-point events in an amount of 7.5% [$0.867 \times 0.660 \times (1.000 - 0.869)$] of the total number of photoabsorption events will be presented in peak 4.

Some primary quanta can be absorbed as a result of two-step process of "Compton scattering-photoeffect". A Compton electron creates one ionization point. A Compton photon absorbed by photoeffect participates in the above-described processes. Therefore, the two-step process makes its contributions to the full-energy peak in the form of two- and three-point events and to peak 4 in the form of two-point events. Upon normalization to the peak area, the estimated final composition of events for the full-energy peak contains 44.1% (single-point events) + 51.2% (two-point events) due to photoeffect + 2.2% (two-point events) + 2.5% (three-point events) due to the two-step process. In peak 4, there are 95.3% single-point events + 4.7% two-point events.

Examples of pulses (dark lines) corresponding to events of two types are presented in Fig.3. The pulse due to photoabsorption of a 88-keV photon with escape of electrons only (a single-point event) is shown in Fig.3a, and simultaneous escape of characteristic photon Kr with an energy of 12.6 keV and a photoelectron ($E_\gamma - E = 88$ keV - 12.6 keV = 75.4 keV (a two-point event) is illustrated in Fig.3b. The maximum distance between pointwise charge clusters in projection onto the counter's radius is equal to the radius. For pure Kr, the evaluated time it takes for ionization electrons to drift from the cathode to the anode is 53 μ s. From Figs.3a and 3b, it is apparent that the second pulse with a $\sim 3 \div 5$ times smaller amplitude is produced in the counter in about ~ 53 μ s after the first one. This pulse is generated by secondary photoelectrons knocked out of the cathode by photons produced during development of an avalanche from the primary ionization. The probability of photoeffect on the cathode is rather high, since the working gas contains no

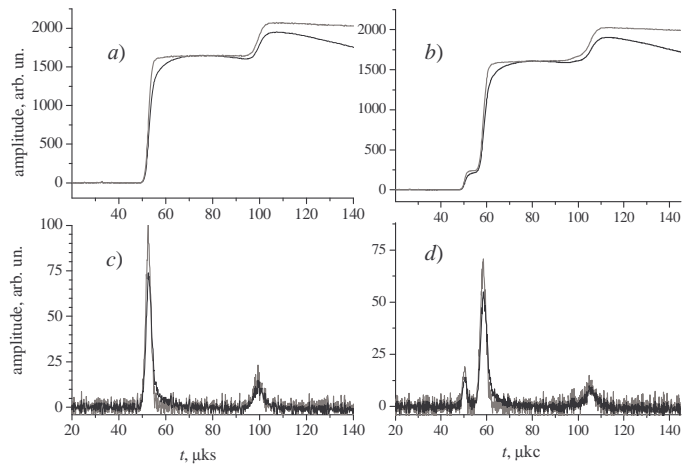


FIG. 3: Examples of pulses (dark lines) of two types of events: (a) for photoabsorption of an 88-keV photon with an escape of electrons only (a single-point event), (b) simultaneous escape of a 12.6-keV characteristic photon $Kr_{K\alpha}$ and a photoelectron ($E_\gamma - E_{KrK\alpha} = 88.0$ keV - 12.6 keV = 75.4 keV (a two-point event)). The calculated, area-normalized current pulses of primary ionization electrons are shown with light lines in Figs. 3c and 3d, while the respective voltage (charge) pulses obtained by integrating these current pulses are depicted with light lines in Figs. 3a and 3b.

quenchers.

III. DETERMINING THE SHAPE OF THE LPC CURRENT SIGNAL

The digitized output pulse from the measuring channel can be presented as direct convolution of sought signal $x(t_i)$ with response pulse \hat{G} from the linear system, which is distorted by stochastic or determinate noise $z(t_i)$:

$$\begin{aligned} y(t_i) &:= \hat{G}x(t_i) + z(t_i), i = 0, \dots, N-1 \\ &:= (g \otimes x)(t_i) + z(t_i). \end{aligned} \quad (1)$$

The noise level determines the lower limit on the sensitivity of the measuring channel, while the instrumental function defines the resolution value.

Given the values of y and \hat{G} , one can try to estimate $x(t)$ in the presence of noise $z(t)$; i.e., in principle, it is possible to state the inverse problem (deconvolution) of determining the signal at the linear system output by the values of the output signal:

$$\tilde{x}(t_i) = \hat{G}^{-1}y(t_i) = x(t_i) + \hat{G}^{-1}z(t_i), \quad (2)$$

where \hat{G}^{-1} is the operator inverse.

To determine the values of charges released in individual clusters of a multipoint event, one can differentiate the original charge pulse ($\hat{G}^{-1} = \frac{d}{dt}$) and represent the obtained shape by a set of Gaussian curves. The evaluated area under an individual Gaussian curve will

correspond to the charge (energy) value in the relevant cluster. From Figs.3c and 3d, it is apparent that direct differentiation provides an asymmetric bell shape (dark line). Such shape results from the nearly Gaussian distribution of the current pulses due to electrons of primary ionization from a pointwise energy deposit, which arrive at the boundary of the gas amplification region near the anode wire.

This shape is determined by the spatial distribution of the charge density in projection onto the radius. The parameters of this distribution depend on the time it takes for the primary charge cluster to drift to the anode. As it drifts, the charge cluster spreads out into a cloud due to electron diffusion. The pulse read out from the anode wire is mostly produced by a negative charge induced on the anode moving toward the cathode by positive ions produced near the wire in gas amplification process and moving toward the cathode i.e., the ion component (i.c.). The estimated total ion drift time is 0.447 s. The contribution of the equilibrium (with ions) electron component (e.c.) to the total induced charge is $\sim 7\%$. The electron collection time is ~ 1 ns.

The output pulse shape is defined by the superposition of induced charges from single electron avalanches distributed in time and intensity according to: the shape of the current pulse from primary ionization electrons, the shape of a pulse from an individual avalanche, and a finite time of the CSA self-discharge. The last two parameters are responsible for the asymmetry of the output current pulse. The output current pulse can be transformed to a symmetric shape by taking into account the analytical dependence of the amplitude of the output voltage pulse generated by a point (in projection onto the radius at the boundary of the gas amplification region) group of primary ionization electrons as a function of time and discharge constant of the output storage capacitor [15]:

$$V_k(t_i) = K_{i.c.} n_k \exp\left(-\frac{t_i + B}{RC}\right) \times \left\{ \ln\left(1 + \frac{t_i}{B}\right) + \frac{t_i}{RC} + \frac{t_i^2}{2 \cdot 2!(RC)^2} + \dots \right\} + K_{e.c.} n_k \exp\left(-\frac{t_i}{RC}\right), \quad (3)$$

where $V_k(t_i)$ is the amplitude of the voltage pulse from the k th group of electrons, n_k is the number of primary electrons in the k th group, $t_i = t(t_0 + t_{i0})$ is the current time for the dependence of the voltage pulse amplitude from the k th group, t_0 is the time of origin of the total pulse, and t_{i0} is the time of origin of the pulse from the k th group, $K_{i.c.} = MV_{(1)i.c.}$, M is the gas amplification factor,

$$V_{(1)i.c.} = (e/C) \cdot \ln(r_k/r_0) \ln(r_k/r_a)$$

is the total voltage pulse amplitude produced at output capacitor C by a single ion generated in the gas discharge, e is the electron charge, r_0 is the radius corresponding to the avalanche's center of gravity, r_a is the

anode radius, r_k is the cathode radius, B is the time parameter associated with the motion of positive ions of the gas discharge in a particular gas (for the LPC filled with Kr at 4.51 at, $B = 2.28$ ns), $RC = \tau_d$ is the CSA discharge constant, R is the leakage resistance, $K_{e.c.} = MV_{(1)e.c.}$, and

$$V_{(1)e.c.} = (e/C) \cdot \ln(r_0/r_a) \ln(r_k/r_a)$$

is the total voltage pulse amplitude produced at output capacitor C by a single electron generated in the gas discharge. In Eq.(3), the electron component is assumed to appear instantly.

At $\tau_d = \infty$, Eq. (3) assumes the form

$$V_k(t_i) = K_{i.c.} n_k \times \ln\left(1 + \frac{t_i}{B}\right) + K_{e.c.} n_k. \quad (4)$$

In our case, $\tau_d \approx 192 \mu s$. For a time interval satisfying condition $t/\tau_d < 2$, Eq. (3) can be reduced to the first two expansion terms.

If it is assumed that the gas discharge from n_k of primary electrons happens at the beginning of the digitization interval, the pulse amplitude at the end of this interval can be described by Eq. (3) for $t = 160$ ns, since the influence of the output capacitor discharge over this time is negligible. If a contribution of the earlier discharges is absent in this time interval, the pulse amplitude at the upper bound of the interval can be used to determine the n_k value. In this case, it is taken into account that, at the end of a 160-ns interval, the contributions of the terms to the total $V_k(t_i)$ value in Eq. (3) make 74 and 26%, respectively. These conditions are satisfied in the recorded actual pulse in the first time channel from the beginning of the pulse. The n_1 value obtained from the actual pulse is used in Eq. (3) to calculate the total shape of the partial pulse in the entire time interval from the beginning to the end of the frame. The pulse obtained thereby is subtracted from the actual one. Therefore, the above condition is now fulfilled for the first digitization interval of the residual pulse or for the second interval of the original pulse. This procedure is repeated until the last time channel in the frame.

The sequence of n_k values for a single-point event has a symmetrical distribution with a nearly Gaussian shape. It is this distribution that is used for further analysis. The area under the Gaussian curve or, in the case of a multiparticle event, the sum of the Gaussian areas on a time interval of $53 \mu s$ from the beginning of the pulse yields the total number of primary ionization electrons. To plot the spectra in Fig.2, this sum is multiplied by the coefficient equal to the averaged ratio of areas of the actual current pulse and of the calculated Gaussian curve for purely single-point events.

The calculated, area-normalized current pulses of primary ionization electrons at the boundary of the gas amplification region are shown with light curves in Figs.3c and 3d, and the corresponding voltage (charge) pulses obtained by integrating these current pulses are depicted with light lines in Figs 3a and 3b.

From Figs.3c and 3d, it is apparent that, at an energy deposit of 88 keV, the signal-to-noise ratio (SNR) is rather high. In the energy range of $20 \div 30$ keV, in which the $2K$ -capture in ^{78}Kr is sought, the SNR for individual components of the total energy deposit corresponding to the possible effect (25.3 keV) is not so favorable.

Figures 4a and 4b present examples of recalculated current pulses for two types of two-point energy deposits due to the K -capture of ^{81}Kr isotope. The total energy deposit corresponds to the binding energy of an electron in the K -shell of a daughter ^{81}Br (13.5 keV). The energies of a characteristic quantum ($E_{K\alpha} = 11.9$ keV) and concomitant Auger electrons ($E_a = 1.6$ keV) are close to the energies of individual components for events of the $2K$ -capture of ^{78}Kr . More detailed information on the ^{81}Kr source is given in what follows.

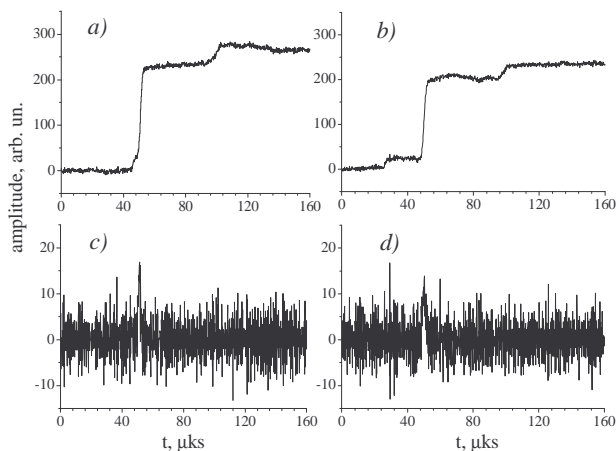


FIG. 4: Primary ionization signals for two types of two-point energy deposits from K -capture of ^{81}Kr isotope accompanied by an escape of a characteristic photon and a concomitant Auger electron: (a, b) recalculated voltage (charge) pulses and (c, d) corresponding current pulses from primary ionization electrons.

From Fig.4, it is apparent that these signals have a high noise level. Noises and possible electric pickup may both mask the low-energy component and create a false one. The use of traditional methods of frequency filtering with different window functions, e.g., in the form of the Hamming [16], Wiener [17], and Savitzky-Golay [18] filters, sometimes fail to ensure reliable extraction of closely spaced (Fig. 4a) and masking each other components of a compound event.

IV. WAVELET-BASED FILTER

Mathematical studies carried out in late 1980s initiated intense development of a principally new class of orthogonal transforms based on the use of wavelet functions [19]. Wavelet transforms are distinguished by a high degree of locality of their base functions both in the time and frequency regions, which allows one to use them for

processing of many nonstationary processes. "In the preliminary processing of our LPC data it is expedient to use multiresolutional signal analysis [20] based on the *dyadic transform of discrete signals*, and often called discrete wavelet transform (DWT). In this case, the analyzed signal $\tilde{x}(t)$ is presented as the decomposition

$$x^J(t) = \sum_{m=0}^{N_{j_0}-1} \hat{a}_{j_0,m} \varphi_{j_0,m}(t) + \sum_{j=j_0}^J \sum_{m=0}^{N_j-1} \hat{d}_{j,m} \psi_{j,m}(t), \quad (5)$$

where are the well-known orthonormal scaling (scaling functions) and wavelet functions- "ancestor" wavelets; $\hat{a}_{j_0,m} = \langle \tilde{x}, \varphi_{j_0,m} \rangle$ are the empirical approximation coefficients and $\hat{d}_{j,m} = \langle \tilde{x}, \psi_{j,m} \rangle$ are the empirical detailing coefficients; $j, m \in \mathbb{Z}$ are the current values of the scale and the shift; $N_{j_0}(N_j)$ is the number of approximation (detailing) coefficients considered at the relevant levels of the decomposition; j_0 is the initial scale value; and J is the final scale value.

Parameter J specifies the resolution of wavelet reconstruction $x^J(t)$ of original signal $x(t)$. Actually, in the case of tendency $J \rightarrow \infty$, the norm tends to $\|x^J - x\| \rightarrow 0$.

Scaling functions $\{\phi_{j,m}(t)\}$ and mother wavelet functions $\{\psi_{j,m}(t)\}_{j,m \in \mathbb{Z}}$, which have $2K$ nonzero coefficients, satisfy the so-called two-level relations [19]:

$$\varphi(t) = \sqrt{2} \sum_{n=0}^{2K-1} h(n) \varphi(2t - n),$$

$$\psi(t) = \sqrt{2} \sum_{n=0}^{2K-1} g(n) \varphi(2t - n),$$

where $h(n)$ and $g(n)$ are the coefficients of low- and high-frequency filters of the wavelet transform, when $g(n) = (-1)^n h(2K - n - 1)$. As distinct from other types of transforms, in which the base functions are explicitly specified, one succeeds in analytically obtaining the base functions in the wavelet analysis only in rare cases, and the basis is most frequently specified by coefficients $h(n)$ and $g(n)$. In this paper, we use wavelets of the Daubechies family. The scaling functions and the Daubechies wavelets are continuous functions that are not identically equal to zero on a finite segment and are not differentiable anywhere on this segment. Table I contains the filter coefficients used in the Daubechies scaling functions *db4* and *db6* (numbers 4 and 6 denote the number of nonzero coefficients in the filters). They are rational numbers and fully define the Daubechies wavelet transform (DWT) [19]. In contrast both to the Fourier transform, which localizes frequencies, but fails to provide time resolution for the process, and to the apparatus of δ -functions, which localizes moments of time, but have no frequency resolution, the DWT makes it possible to reveal the local properties of any structure of an individual event on different scales, eliminating smooth polynomial characteristics and emphasizing fluctuation structures. It

TABLE I: Coefficients of the low-frequency filters for wavelets with compact carriers *db4* and *db6*. The $h(n)$ values are normalized so that $\sum_{n=0}^{2^K-1} h(n) = \sqrt{2}$ [19]

$h(n)$	<i>db4</i> ($K=2$)	<i>db6</i> ($K=3$)
$h(0)$	$(1 + \sqrt{3})/4\sqrt{2}$	$(1 + \sqrt{10} + \sqrt{5 + 2\sqrt{10}})/16\sqrt{2}$
$h(1)$	$(3 + \sqrt{3})/4\sqrt{2}$	$(5 + \sqrt{10} + 3\sqrt{5 + 2\sqrt{10}})/16\sqrt{2}$
$h(2)$	$(3 - \sqrt{3})/4\sqrt{2}$	$(10 - 2\sqrt{10} + 2\sqrt{5 + 2\sqrt{10}})/16\sqrt{2}$
$h(3)$	$(1 - \sqrt{3})/4\sqrt{2}$	$(10 - 2\sqrt{10} - 2\sqrt{5 + 2\sqrt{10}})/16\sqrt{2}$
$h(4)$	–	$(5 + \sqrt{10} - 3\sqrt{5 + 2\sqrt{10}})/16\sqrt{2}$
$h(5)$	–	$(1 + \sqrt{10} - \sqrt{5 + 2\sqrt{10}})/16\sqrt{2}$

is possible to completely eliminate statistical fluctuations by selecting only strong correlated fluctuations, which will allow one to observe exactly those dynamic fluctuations that exceed the statistical component (noise).

A. Noise elimination using the wavelet method

Among the modern noise suppression techniques, the Donoho-Johnstone method has received the widest acceptance [21]. This method is rather simple in implementation and time-saving in computational aspect, since it implies the use of only fast algorithms of wavelet transform. It consists of three steps, which, being successively applied to the original signal, produce a noise-suppression effect. At the first step, signal under investigation $x(t)$ is subjected to DWT; afterward, the threshold noise elimination procedure is applied to each of the detailing coefficients of level j and, sometimes, to the approximation coefficients of the same level; and, finally, inverse wavelet transform is performed, which results in reconstruction of the signal that is characterized, as expected, by a higher SNR.

This technique is a nonparametric estimate of the regression signal model with the use of an orthogonal basis [22]–[24]; it operates with high efficiency with signals in the decomposition of which only a few detailing coefficients significantly differs from zero. Selection of a particular wavelet form depends on the problem under investigation and is not predetermined beforehand [25]. The depth of decomposition generally depends on the properties of the analyzed signal. Smooth wavelets produce a smoother signal approximation, and vice versa—“short” wavelets better search for peaks of the approximated function. The depth of decomposition affects the scale of rejected details; i.e., as the depth of decomposition increases, the model subtracts the noise of a steadily increasing level until the scale of details becomes too large and the transform starts distorting the original signal shape. Upon further increase in the depth of decomposition, the transform starts forming a smoothed version of the original signal; i.e., apart from the noise, some local peculiarities of the original signal are also fil-

tered off. Decomposition of the signal and its reconstruction by the approximation and detailing coefficients that have passed threshold processing is carried out using the Malla algorithm [20] and the lifting procedure [26]. The threshold processing itself is performed with the aid of one of the threshold noise suppression operations. In accordance with the *hard threshold* processing [21], all coefficients $\{\hat{d}_{j,k} | k \in Z\}$ of level j , which are greater than or equal to the threshold, are held constant, while the other coefficients that do not satisfy this condition are reduced to zero:

$$d_{j,k}^h = \hat{d}_{j,k} I\left(\left|\hat{d}_{j,k}\right| > \theta_j\right), \quad \theta_j = \rho_j \sigma_i, \quad (6)$$

where ρ_j is the threshold factor for the specified scale [20], and σ is the noise variance on the j th scale. Hard threshold processing is a straight-out procedure. It should nevertheless be taken into account that a hard threshold has two drawbacks that can lower its usefulness for the noise suppression task. The first consists in the fact that retaining of detailing coefficients above a predetermined threshold value also implies retaining of their noise. The other drawback is in the presence of parasitic harmonics generated in the resulting signal by artificial introduction of lacunas (gaps) formed due to the coefficients reduced to zero. The use of *soft threshold* processing implies recalculation of detailing coefficients d in the following way:

$$d_{j,k}^s = \text{sign}\left(\hat{d}_{j,k}\right) \left(\left|\hat{d}_{j,k}\right| - \theta_{thr}\right), \quad (7)$$

where θ is a certain threshold value.

In this case, apart from the reduction to zero of the coefficients d actually containing only the noise component, the detailing coefficients are decreased by the θ_{thr} value, which corresponds to noise suppression in the informative coefficients as well. Threshold θ_{thr} , which defines the analyzed signal, is a sole parameter that cannot be exactly estimated directly from actual data. Mathematical solutions in determining the threshold value seem unsatisfactory to be a priori accepted. In an ideal case, we tend to specify this threshold so as to minimize the root-mean-square error (rmse):

$$\varepsilon = \sqrt{\frac{1}{N} \sum_{i=1}^N [x(t_i) - \tilde{x}(t_i)]^2}. \quad (8)$$

Therefore, by analogy to [20],[26], we determine the basic signal component relying on threshold processing of the model signal. Ideal threshold processing minimizes the rmse, making all coefficients with the signal component below σ vanish [20]. In other words, it is assumed that the free from noise signal component above σ is an original signal; i.e., $\theta_{thr} = \sigma$. This selection can be tested on the model signals. Our experience gained in working with natural signals confirms that the ratio of the signal peaks to the noise level reaches its maximum near $\theta_{thr} = \sigma$.

B. Test of model signal with noise

To illustrate the efficiency of different approaches to the deconvolution problem, let us select model signal $x(t_n)$, which is specified on a set of points $N = 2^{10}$ and consists of three closely spaced Gaussian peaks

$$a_k \exp(-(t - t_k)^2 / 2\mu_0^2),$$

where $a_k = [1.32, 7.0, 7.0]$, $t_k = [277, 307, 327]$, and $\mu_0 = 7$. Let us add Gaussian noise and a harmonic term to it:

$$\tilde{x}(t_n) = x(t_n) + \kappa\Delta(\tau) + g(t_n),$$

where $\Delta(\tau)$ is ordinary Brownian process analyzed on $\tau \in [0, 1]$, κ is a certain coefficient, and $g(t_n)$ is the harmonic term.

For the variance σ^2 of the noise component in model signal $W(t_n) = \kappa\Delta(\tau) + g(t_n)$ to be estimated by the $x(t_n)$ data, it is necessary that the influence of signal $x(t_n)$ be suppressed. A rough estimate can be obtained from the mean values of the smallest-scale wavelet coefficients [21]. The signal with length N has $N/2$ wavelet coefficients $\{\langle \tilde{x}(t_n), \psi_{j,m} \rangle\}_{0 \leq m \leq N/2}$ of the smallest scale $2^j = 2N^{-1}$. Coefficients $|\langle x(t_n), \psi_{j,m} \rangle|$ are small if signal $x(t_n)$ is smooth on carrier $\psi_{j,m}$, and in this case, $\langle \tilde{x}(t_n), \psi_{j,m} \rangle \approx \langle W, \psi_{j,m} \rangle$. However, if $x(t_n)$ has a sharp differential on carrier ψ , coefficients $|\langle x(t_n), \psi_{j,m} \rangle|$ are rather large. In the case of a piecewise-smooth signal, we have several differentials, which results in a certain number of large coefficients. This number is small in comparison with $N/2$. At the smallest scale, signal $x(t_n)$ defines the value of a small portion of large-amplitude coefficients $|\langle x(t_n), \psi_{j,m} \rangle|$, which are considered to be "overshoots". All the other coefficients are approximately equal to $\langle W, \psi_{j,m} \rangle$; they are independent random Gaussian variables with variance σ^2 . Therefore, σ^2 can be roughly estimated, with the influence of $x(t_n)$ being ignored, by the mean of absolute values $\{|\langle \tilde{x}(t_n), \psi_{j,m} \rangle|\}_{0 \leq m \leq N/2}$, divided by 0.6745 [22].

Daubechies filters *db4* were used in a direct wavelet transform and when the estimate of the useful signal was synthesized from coefficients after their threshold processing, whereas higher-order filters *db6* were employed to estimate the threshold values.

Calculations of all wavelet coefficients, testing of the noise suppression algorithms, and selection of required signals for further analysis were performed using MATLAB and its web libraries [27].

The results are shown in Fig.5. It is apparent that all filters provide good noise suppression efficiency (the SNR is > 30 dB), but the signals passed through the wavelet filters with the use of the hard or soft threshold processing better represents the shape of the original signal (Figs.5e and 5f), which ensures more reliable signal resolution into individual components. For our purposes, hard threshold processing is quite satisfactory both in the quality factor and in the computational time.

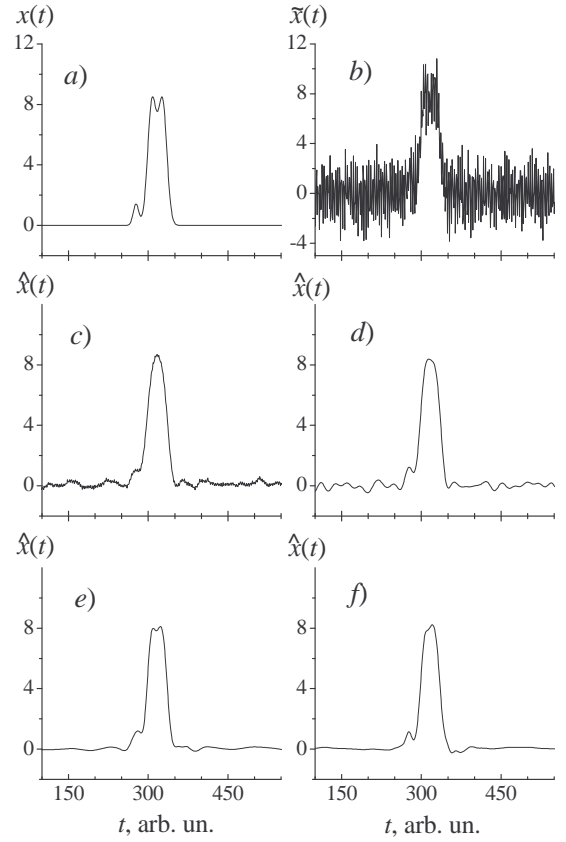


FIG. 5: (a) Model signal from three closely spaced Gaussian peaks; (b) additive mixture of the model signal with noise; noise suppression using (c) the Savitzky–Golay filter and (d) Wiener filter; (e, f) Daubechies wavelet filters, *db4*, with hard and soft threshold processing, respectively.

V. RELIABILITY IN IDENTIFYING MULTIPOINT EVENTS

In order to verify the efficiency of the algorithm for the noise suppression and pulse shape discrimination for multipoint events from an actual source the LPC was filled with natural Kr containing cosmogeneous radioactive isotope ^{81}Kr ($T_{1/2} = 2.1 \times 10^5$ yr) with a bulk activity of $\sim 0.1 \text{ min}^{-1} l^{-1} \text{Kr}$ [28], [29]. It decays by electron capture into $^{81}\text{Br}^*$. In 87.5% of cases, an electron is captured from the *K*-shell of a Kr atom (*K*-capture) [30]. Filling of the vacancy at the *K*-shell of a daughter Br atom is accompanied in 61.4% of cases by an escape of two characteristic quanta with energies of 11.92 keV ($K_{\alpha 1}$, 100%), 11.88 keV ($K_{\alpha 2}$, 50.9%), 13.29 keV ($K_{\beta 1}$, 21.0%), and 13.47 keV ($K_{\beta 2}$, 1.07%) [12] and concomitant Auger electrons with energies of 1.55 keV, 1.60 keV, 0.27 keV, and 0.01 keV, respectively (the relative intensities of $K_{\alpha,\beta}$ lines are presented in brackets). From this list, it is apparent that, when photons $K_{\alpha 1}$ and $K_{\alpha 2}$ escape, the energy of Auger electrons is sufficient for a distinguishable two-point event to be formed. In 38.6% of cases, filling of the vacancy at the *K*-shell of Br is accom-

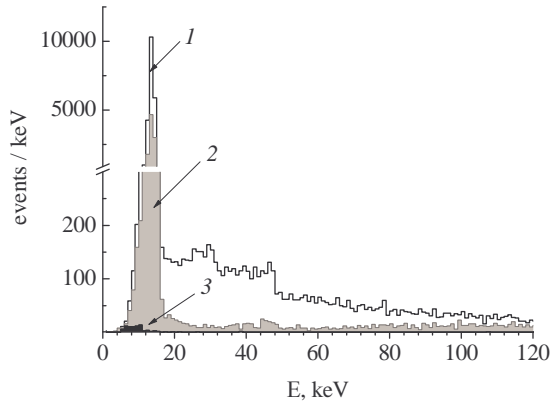


FIG. 6: Amplitude spectra (1) of single-, (2) two-point, and (3) three-point events that form the total analyzed pulse amplitude spectrum of the counter detecting both background and ^{81}Kr decays.

panied by an escape of a cascade of Auger electrons that produce a single-point energy deposit. Events with an escape of characteristic photons $K_{\beta 1}$ and $K_{\beta 2}$ should also be placed into a category of single-point events. Taking into account the absorption efficiency for characteristic photons in the LPC working gas ($\epsilon_{abs} = 0.869$) and using the above data, one can calculate the composition of a 13.5-keV full-energy peak: 49.4% of all events are single-point, and 50.6% are two-point.

Describing the noise-free signals by a set of Gaussian curves using rmse minimization technique (7), one can discriminate between two- and single-point events. Figure 6 presents the energy spectra (1) of single-, (2) two-, and (3) three-point events forming the total analyzed pulse-amplitude spectrum of the counter that detects both background and ^{81}Kr decays. Similar components (spectra 1-3) of total spectrum 1 for a calibration measurement of 88-keV γ rays are shown in Fig.2.

Given the composition of events from the ^{81}Kr and ^{109}Cd sources and results of simulation of these processes in the LPC, one can, using the GEANT 4.8.2 program [31], determine the quality of suppression of the noise component and the efficiency of the procedure for separating events by the criteria of a multipoint event. Table II presents the percentage composition of three types of events in the full-energy peaks with energies of 13.5 keV (^{81}Kr) and 88 keV (^{109}Cd), which was obtained by estimation (column I); by simulation of processes in the LPC, ignoring the confluence of closely spaced primary charge clusters (column IIa), and taking into account their confluence (column IIb); and by separation of the experimental spectrum into components after its wavelet purification of noise using hard threshold processing (column III).

Determining the parameters of individual components in a compound event, it is possible to perform energy calibration in the energy range under investigation and determine the energy resolution of single-point components which form a multipoint event. The energy dis-

tributions of individual components of two-point events from the ^{81}Kr and ^{109}Cd sources are shown in Figs. 7 and 8, respectively.

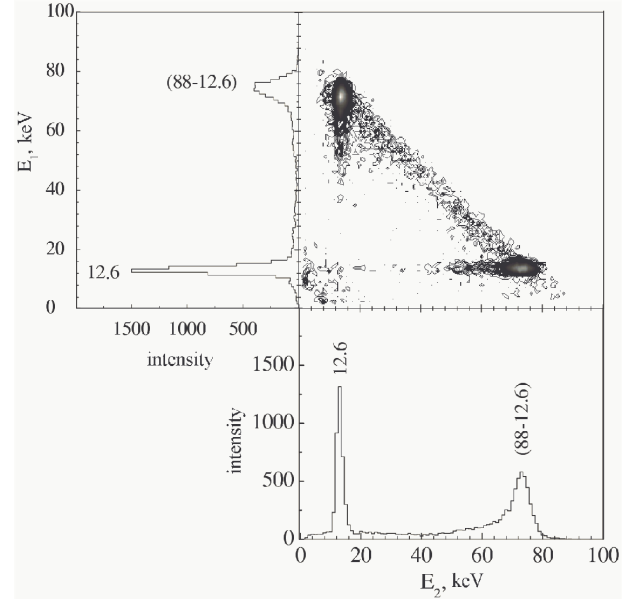


FIG. 7: Amplitude distributions of energy deposits of individual components for two-point events from the source placed in the middle of the LPC length (^{109}Cd).

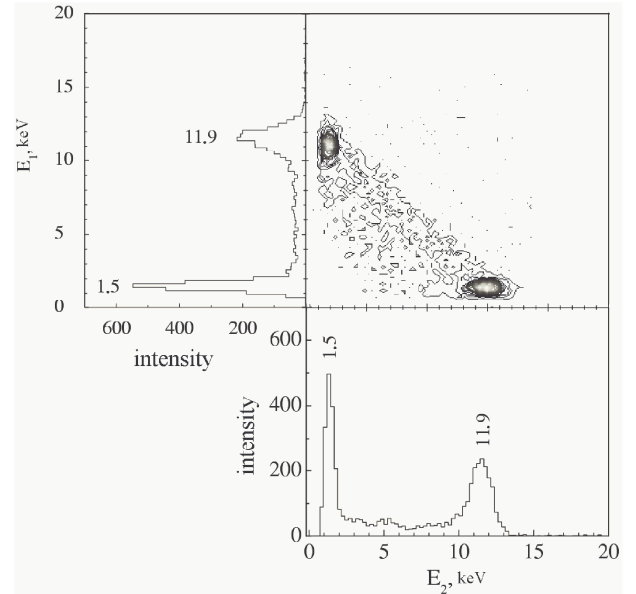


FIG. 8: Amplitude distributions of energy deposits in of individual components of for two-point events from the internal (^{81}Kr) source with a total energy of 13.5 keV.

VI. CONCLUSIONS

The analysis both of the pulse shape variety and methods of LPC signal processing has been performed using a multiresolutional wavelet analysis. It has been shown that the noise component can be suppressed successfully, and the problem of separating of the events with closely spaced clusters, partially or fully lapping over each other, can be solved with a high efficiency, and the parameters of these events can be estimated. The test measurements of signals from the krypton-filled LPC irradiated by in-

ternal and external sources have made it possible to determine the efficiency of discrimination between single-, two-, and three-point events. The described technique helps increase the sensitivity of detection of compound events in gas-filled detectors and demonstrates its applicability to detection of rare events from $2K(2\nu)$ capture in large proportional counters.

Acknowledgments. The work has been carried out under the financial support of the RFBR (grant no. 04-02-16037) and "Neutrino Physics" Program of the Presidium of RAS.

TABLE II: Relative composition of three types of events in the full-energy peaks with energies of 13.5 keV (^{81}Kr) and 88 keV (^{109}Cd), obtained by estimation (column *I*); by simulation of processes in the LPC, ignoring the confluence of closely spaced pointwise ionization regions (column *IIa*) and taking into account their confluence (column *IIb*); and by separation of the experimental spectrum into components after its wavelet purification of noise using hard threshold processing (column *III*).

type of events	13.5 keV (^{81}Kr)				88 keV (^{109}Cd)			
	calc., % <i>I</i>	GEANT4.8.2, % <i>IIa</i>	empiric., % <i>IIb</i>	empiric., % <i>III</i>	calc., % <i>I</i>	GEANT4.8.2, % <i>IIa</i>	empiric., % <i>IIb</i>	empiric., % <i>III</i>
singl-point	49.4	44.1	66.2	68.2	44.1	45.0	59.4	56.8
two-point	50.6	55.9	33.8	31.7	53.4	53.7	40.0	39.4
three-point				< 0.1	2.5	1.3	0.6	3.4

-
- | | |
|---|--|
| <p>[1] V.I. Tretyak and Y. G. Zdesenko, At. Data Nucl. Data Tables 80, 83 (2002).</p> <p>[2] A.S.Barabash, Czech.J.Phys. 52, 567 (2002).</p> <p>[3] C. Cremonesi, Int. J. Mod. Phys. A21 (2006) 1887.</p> <p>[4] Danevich, F.A., Kobychiev, V.V., Nagorny, S.S., and Tretyak, V.I., NIM Phys. Res, 2005, vol. A544, p.553.</p> <p>[5] Barabash, A.S., Hubert, Ph., Nachab, A., et al, Nucl. Phys. A, 2008, vol. 807, p. 269; Nucl. Phys. A, 2007, vol. 785, p. 371; J. Phys. G, 2007, vol. 34, p. 1721.</p> <p>[6] Rukhadze, N.I., Benes, P., Briancon, Ch., et al., Bull. Rus. Acad. Sci. Phys, 2008, vol. 72, p. 731.</p> <p>[7] Gavriljuk, Ju.M., Kuzminov, V.V., Osetrova N.Ya., and Ratkevich S.S, Phys. Atomic Nucl., 2000, vol. 63, p. 2201.</p> <p>[8] Aunola, M. and Suchonen, J., Nucl. Phys. A., 1996, vol. 602, p. 133.</p> <p>[9] Hirsch, M., Muto, K., Oda, T., and Klapdor-Kleingrothaus, H.V., Z. Phys. A, 1994, vol. 347, p. 151.</p> <p>[10] Rumyantsev, O.A. and Urin, M., Phys. Lett.B, 1998, vol. 443, p. 51.</p> <p>[11] Doi, M. and Kotani, T., Prog. Theor. Phys., 1992, vol. 87, p. 1207.</p> <p>[12] Blokhin, M.A. and Shveitser, I.G., Rentgenospektral'nyi spravochnik (Handbook on X-ray Spectra), Moscow: Nauka, 1982.</p> <p>[13] Storm, A. and Israel, H., Secheniya vzaimodeistviya gamma-izlucheniya (Cross Sections of the Gamma-Radiation), Moscow: Atomizdat, 1973.</p> <p>[14] Blokhin, M.A. and Shveitser, I.G., Rentgenospektral</p> | <p>nyi spravochnik (Handbook on X-ray Spectra), Moscow: Nauka, 1982.</p> <p>[15] Abramov, A.I., Kazanskii, Yu.A., and Matusevich, E.S., Osnovy eksperimental'nykh metodov yadernoi fiziki (Bases of the Experimental Methods of Nuclear Physics), Moscow: Energoatomizdat, 1985.</p> <p>[16] Hamming, R.W., Digital Filters., (Englewood Cliffs), NJ: Prentice-Hall, 1983.</p> <p>[17] Hillery, A.D. and Chin, R.T., IEEE Trans. Signal Proc., 1991, vol. 39, p. 1892.</p> <p>[18] Savitzky, A. and Golay, M.J.E., Anal. Chem., 1966, vol. 36, p. 1627.</p> <p>[19] Daubechies, I., Ten Lectures on Wavelets, Philadelphia: SIAM, 1992. wavelet representation., IEEE Trans. Pattern Anal. and Machine Intel., 1989, vol. 11, no. 7, pp. 674.</p> <p>[20] Mala, S., Veivlety v obrabotke signalov (Wavelets in Signal Processing), Moscow: Mir, 2005.</p> <p>[21] Donoho, D. and Johnstone, I., Biometrika, 1994, vol. 81, p. 425.</p> <p>[22] Donoho, D.L. and Johnstone, I.M., J. Amer. Stat. Assoc., 1995, vol. 90, no. 432, p. 1200; Neumann M., J. Time Series Analysis, 1996, vol. 17, p. 601.</p> <p>[23] Abramovich, F., Bailey, T.C., and Sapatinas, T., The Statistician, 2000, vol. 49, p. 1.</p> <p>[24] Neumann, M. and Sachs, R., Annals of Statistics, 1997, vol. 25, p. 38.</p> <p>[25] Ratkevich, S.S., Vestnik Kharkovskogo Nats. Univ., Ser. Fiz. Yadra, Chastitsy, Polya, 2006, no. 746, issue 4, p.</p> |
|---|--|
-

- 23.
- [26] Sweldens, W., SIAM J. Math. Anal, 1996, vol. **3**, no. **2**, p. 186.
- [27] <http://www-stat.stanford.edu/~wavelab/>;
<http://www-dsp.rice.edu/software/rwt.shtml>
- [28] Loosli, H.H. and Oeschger, H., Earth Planet. Sci. Lett., 1968, vol. **7**, no. **1**, p. 67.
- [29] Kuzminov, V.V. and Pomansky, A.A., Radiocarbon, 1980, vol. **22**, no. **2**, p. 311.
- [30] Chew, W.M., Xenoulis, A.C., Fink, R.W., et al., Nucl. Phys. A., 1974, vol. 229, no. 1, p. 79.
- [31] GEANT–Detector Description and Simulation Tool. CERN Program Library Long write-up, **W5013**, CERN, 1994. <http://geant4.web.cern.ch/geant4/>